Earth Planet. Sci. Lett. 631 (2024) 118624

Contents lists available at ScienceDirect

Earth and Planetary Science Letters

journal homepage: www.elsevier.com/locate/epsl

Declining magma supply to a poroelastic magma mush explains long-term deformation at Soufrière Hills Volcano

Rami Alshembari [a,*], James Hickey [a], Karen Pascal [b,c], Racquel Syers [b]

[a] Department of Earth and Environmental Sciences, University of Exeter, Penryn, Cornwall, TR10 9FE, UK
[b] Montserrat Volcano Observatory (MVO), Flemmings, Montserrat
[c] Seismic Research Centre, University West Indies, Republic of Trinidad and Tobago

ARTICLE INFO

Editor: Dr C. M. Petrone

Keywords:
Volcanology
Geodesy
Geophysics
Magma-mush
FEM, Soufrière Hills Volcano

ABSTRACT

Volcano deformation studies traditionally consider melt-dominated magma reservoirs, often overlooking the significant role of poroelastic mush in modifying surface deformation. Here, we analyze the deformation of Soufrière Hills Volcano (SHV) with a focus on a mush-dominated, poroelastic magma reservoir, drawing on temporal deformation data from 14 continuous GPS stations during the ongoing intra-eruptive unrest period. We implemented a 3D Finite Element model and optimization to simulate the observed deformation. Our results reveal that the deformation is likely driven by ongoing, melt injection ($Q = 1.1\ m^3\ sec^{-1}$) into a low permeability ($k = 4.7 \times 10^{-16}\ m^2$) reservoir with the injection to the base of the reservoir at 16.5 km depth below sea level. Our findings highlight temporal variations in the melt injection rate to fit the decreasing GPS-recorded deformation rates. An initial injection rate $Q_i = 1.9\ m^3\ sec^{-1}$ inferred at the start of our study period decreases to $Q_f = 0.3\ m^3\ sec^{-1}$ over a 12-year period (2010–2022). Exploratory forward modeling suggests that if current trends continue, the end of magma supply to our modelled reservoir could occur around June 2024 ± 2 years. However, this does not imply the end of associated volcanic hazards at SHV, as the poroelastic diffusion of melt will continue, causing redistribution of melt, surface deformation, and potentially initiating reservoir rupture. While our models offer new insights, inherent limitations in our simulations include interdependencies among our explored model parameters that would benefit from further refinement. Despite these limitations, the study offers crucial guidance on understanding and forecasting volcano deformation dynamics, particularly for volcanoes like SHV with crystal-rich magma reservoirs.

1. Introduction

Volcano deformation studies are essential for monitoring and understanding subsurface processes within the Earth's crust. Volcano surface deformation is mainly caused by melt movement within the crust, leading to swelling and/or subsidence of a volcano's surface (Cayol et al., 2022; Dzurisin, 2006; Phillipson et al., 2013; Pritchard et al., 2019; Segall, 2010). Analysis of deformation data collected through advanced geodetic techniques, such as InSAR, GPS, and tiltmeters, provides insights into magma reservoir dynamics (Cayol et al., 2022; Segall, 2019). By analyzing these data, we can identify and quantify the processes driving volcanic deformation, thereby enhancing our capability to assess volcanic hazards and forecast future eruptions to improve volcanic risk mitigation (Segall, 2013). Commonly-used deformation models, based on melt-dominated magma reservoirs, have been challenged by a wealth of observations suggesting that magmatic systems are more complex and heterogeneous, involving crystal-rich magma mushes (Cashman et al., 2017; Edmonds et al., 2019; Sparks et al., 2019). Recent studies propose that magma mushes are better modelled as poroelastic materials in response to melt injection/-withdrawal (Alshembari et al., 2022a; Liao et al., 2018; Mullet and Segall, 2022). Unlike commonly-used models for volcanic surface deformation, poroelastic mush-derived surface deformation continues even after melt supply has ended, owing to continuous poroelastic diffusion of the melt through the system. This post-intrusion deformation evolves at decreasing rates proportional to the mush hydraulic diffusivity (Alshembari et al., 2023; 2022a).

We utilize the concept of mush poroelasticity for analyzing real deformation data from ongoing volcanic unrest, specifically at Soufrière Hills Volcano (SHV) in Montserrat, West Indies (Fig. 1). SHV began its

* Corresponding author.
E-mail address: ra500@exeter.ac.uk (R. Alshembari).

https://doi.org/10.1016/j.epsl.2024.118624
Received 31 August 2023; Received in revised form 22 January 2024; Accepted 17 February 2024
Available online 4 March 2024

current eruptive episode in 1995, characterized by lava dome formation and collapse (Wadge et al., 2014), and offers an ideal opportunity to apply poroelastic mush models to its current deformation as petrological and geophysical investigations suggest an extensive igneous mush system beneath the edifice (Paulatto et al., 2012). Petrological studies on SHV emphasize interactions between newly introduced hydrous basaltic magma (crystal-free) and a shallow andesitic magma reservoir rich in crystals (Barclay et al., 2010; Christopher et al., 2015; Devine and Rutherford, 2014; Edmonds et al., 2016; Zellmer et al., 2003). Paulatto et al. (2012, 2022) struggled to find large melt-rich magma bodies using integrated models that combine seismic tomography and thermal numerical modeling techniques. The average melt fraction at SHV derived from P-wave velocity reduction analysis suggests a value no greater than 12% within a mush region spanning 4–6 km in diameter. However, when incorporating thermal models of crystallization, the melt fraction in the mush region could potentially reach up to 35% (Annen et al., 2014; Paulatto et al., 2012). Thus, given the abundance of evidence supporting a mush state of the igneous system at SHV, it presents an ideal opportunity to explore surface deformation from melt injection into a mush reservoir using poroelasticity theory.

From 1995 onwards, the deformation data from SHV indicate cyclic behavior in the andesitic magmatic system, with the current intra-eruptive repose period being the longest on record since the last eruption ended in February 2010 (Hickey et al., 2022; Odbert et al., 2014). Continuous GPS (cGPS) recordings show island-wide inflation since 2010 with a decreasing deformation rate (Fig. 1), accompanied by steady SO_2 emissions and swarms of volcano-tectonic seismic events (Christopher et al., 2015). The extended duration of the current repose period raises questions about whether it is temporary or signifies the conclusion of the eruptive episode. The uncertainty is compounded by the presence of surface deformation, which has been suggested to be caused by continued magma supply but only through the use of deformation models representing the magmatic system as a pressurized cavity and neglecting any internal (poroelastic) reservoir processes (Hickey et al., 2022).

We analyze temporal deformation data from 14 continuous GPS (cGPS) stations to gain insights into the behavior and evolution of the SHV magmatic system since 2010 and the characteristics of its current period of repose. We employ geodetic numerical models to investigate the role of poroelastic mush behavior in contributing to the current long-term surface inflation. Our approach furthers our understanding of the underlying processes and mechanisms driving observed volcanic activity and deformation patterns.

2. Materials and methods

2.1. Poroelastic magma mush deformation modeling

Magma reservoirs with a high degree of crystallinity are more accurately represented as a porous medium with a poroelastic response to melt injection and withdrawal events (Marsh, 1981; Rosenberg and Handy, 2005; Rutter and Neumann, 1995). As magma cools and reaches a critical crystallinity, crystals form a continuous framework, creating a crystal mush mixture with interstitial melt. This crystal mush can sustain and transmit stress, resisting deformation, while the liquid fraction flows and percolates through the mush, following Darcy's law for fluid flow in porous media.

To model the mechanical response of a poroelastic mush to melt intrusion events, we adapted the linear poroelasticity theory for a homogeneous isotropic, fluid-saturated porous medium (Biot, 1941).

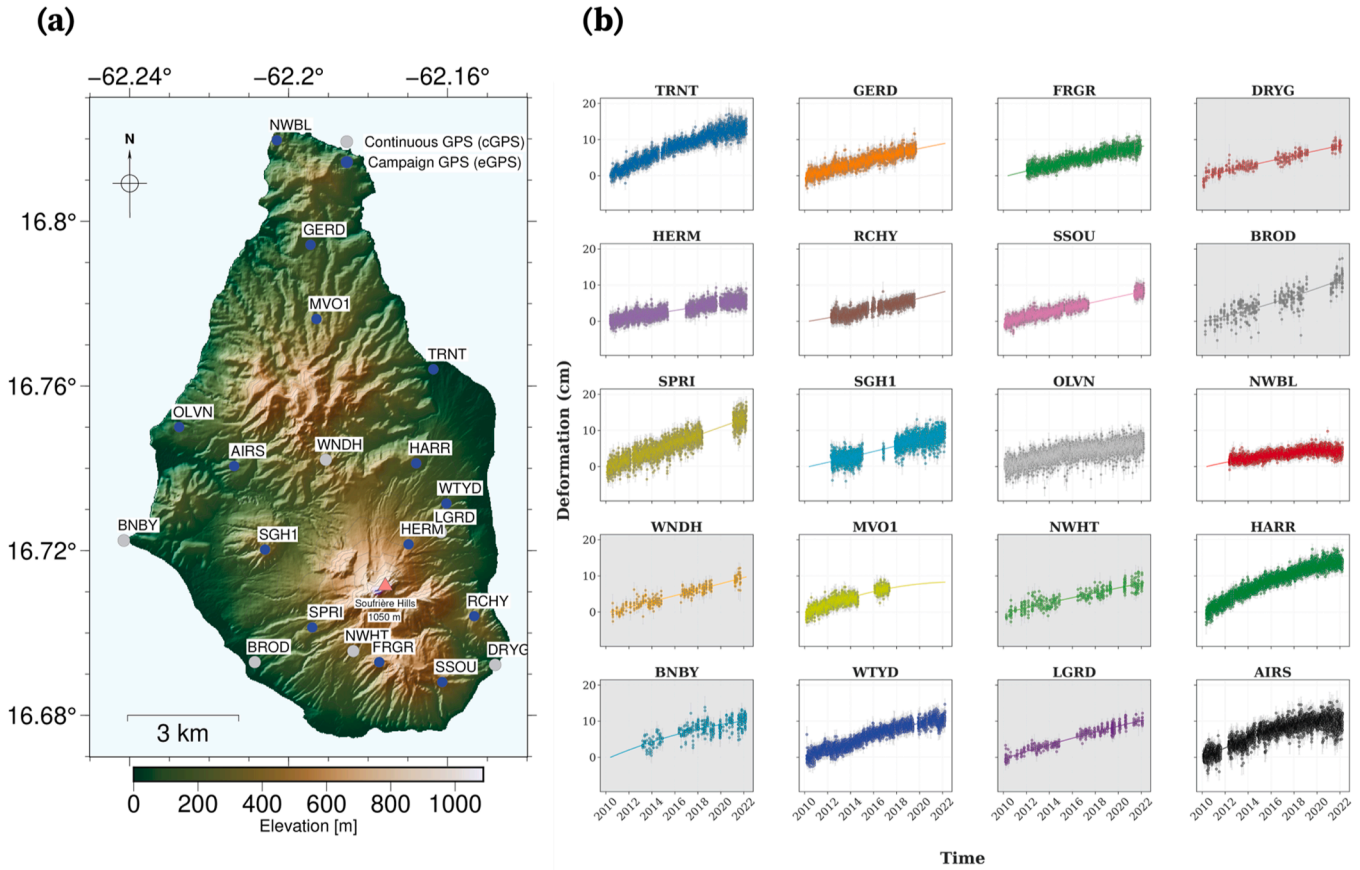

Fig. 1. Continuous GPS (cGPS) and campaign GPS (eGPS) network and vertical deformation at Montserrat. (a) Digital elevation model (DEM) map of Montserrat displaying cGPS stations (blue circles), eGPS stations (grey circles), and active vent (red triangle), with contour intervals of 100 m. (b) island-wide vertical deformation recordings for the period from 2010-02-13 to 2022-03-21, with grey plots representing the results from the eGPS.

Poroelasticity theory encompasses the elastic deformation of the crystal matrix and the flow of interstitial melt (Manga, 2018). Mush reservoir deformation is coupled with the elastic surrounding solid rock.

The constitutive relations for an ideal isotropic poroelastic that relates the strain ε_{ij}^{m} and the stress σ_{ij}^{m} in the poroelastic mush is given by:

$$\sigma_{ij}^{m} = \left(K_d - \frac{2G_d}{3}\right)\delta_{ij}\varepsilon^{m} + 2G_d\varepsilon_{ij}^{m} - \alpha\delta_{ij}P_m \tag{1}$$

where ε^{m} is the mush volumetric strain, K_d is the drained bulk modulus, G_d is the drained shear modulus, δ_{ij} is the Kronecker delta and α is the Biot Willis coefficient. P_m is the mush pore pressure (Bachrach, 2011; Detournay and Cheng, 1994).

Melt flow in the mush follows Darcy's law, which measures the flow in porous media due to gradients in pore pressure:

$$\overrightarrow{q} = -\frac{k}{\eta_m}\nabla P_m \tag{2}$$

where $\overrightarrow{q}$ is the Darcy velocity of the melt, k is the crystalline skeleton permeability, η_m is the interstitial melt dynamic viscosity and ∇P_m is the pressure difference in the mush.

When modeling surface deformation while considering the poroelastic behavior of magma mush subjected to melt injection events, the resulting surface deformation depends on the mush's hydraulic properties (Alshembari et al., 2022a). Deformation magnitude and rate are proportional to the hydraulic diffusivity, expressed as:

$$c = \frac{k}{\mathrm{S}\,\eta_m}, \tag{3}$$

where S is the storage coefficient, which is dependent on the mechanical properties of the mush and given by:

$$S = \varnothing X_f + (\alpha - \varnothing)\frac{(1-\alpha)}{K_d} \tag{4}$$

where X_f is the interstitial melt compressibility and ϕ is the mush porosity (or melt fraction).

We consider a linear elastic model domain surrounding the magma reservoir. Deformation of the surrounding rock is produced by the stress induced by melt diffusion in the reservoir and is linked by the constitutive relation for a linearly elastic solid:

$$\sigma_{ij}^{R} = \left(K_R - \frac{2G_R}{3}\right)\varepsilon_{ij}^{R} + 2G_R\varepsilon^{R}, \tag{5}$$

where σ_{ij}^{R}, ε_{ij}^{R} and ε^{R} are the stress and strain tensors, and the volumetric strain, respectively, of the rock, *R*. K_R and G_R are the bulk and shear moduli of the surrounding rock.

2.2. Model formulation

We employ finite element method (FEM) numerical models to determine the elastic stresses and associated deformation field generated in a mechanically heterogeneous model domain due to a mush-dominated magma reservoir undergoing melt resupply. The calculations are performed using COMSOL Multiphysics® v5.6, utilizing a 3D model domain within the structural mechanics and subsurface flow modules. Further similar detailed model descriptions are available in Alshembari et al. (2022a).

The model domain is partially-surrounded by an infinite-element domain to prevent boundary effects at the model base and lateral extents. The top of the model domain is a free surface, which is allowed to deform. Conversely, the bottom boundary has a fixed constraint, meaning it is unmovable and maintains its position and shape, representing an anchor point for the model domain. Digital elevation model topography data (Stinton, 2015) from Montserrat is employed to define the upper boundary surface of the 3D model (Fig. 2a). Within the 3D numerical domain, a homogeneous partially crystalline triaxial ellipsoidal reservoir with semiaxes a, b, and c is embedded in an elastic mechanically heterogeneous model domain (Fig. 2c). The preliminary values for the reservoir dimensions are derived from earlier geodetic studies at SHV, suggesting a semi-minor axis of 1.9 km and semi-intermediate axis of 2.0 km horizontally, and semi-major axis of 5.0 km vertically (Gottsmann et al., 2020b; Hickey et al., 2022; Johnson et al., 2023). The vertically elongate reservoir geometry captures the likely presence of a trans-crustal magmatic-mush system, and may incorporate the potential for multiple, smaller, vertically-offset reservoirs (e.g., Elsworth et al., 2008) but with fewer model parameters. Separately testing the impact of multiple discrete mush-dominated reservoirs was beyond the scope of this study, especially given the considerable uncertainty in how they may, or may not, be hydraulically connected.

The mechanical properties of our model domain are obtained from a 3D seismic P-wave (V_P) tomography model, which is based on in-situ observations (Paulatto et al., 2012). We convert V_P values into a dynamic Young's Modulus (E_D) and density (ρ_R), following the approach of (Brocher, 2005).

$$\rho_R = 1.6612\mathrm{v_p} - 0.4721\mathrm{v_p^2} + 0.0671\mathrm{v_p^3} - 0.0043\mathrm{v_p^4} + 0.000106\mathrm{v_p^5} \tag{6}$$

$$E_D = \frac{v_p^2\rho(1+\nu)(1-2\nu)}{(1-\nu)} \tag{7}$$

where ν is the Poisson's Ratio of 0.25. We converted dynamic Young's modulus (E_D) to static Young's modulus (E) using a conservative scaling factor of 2 ($E = \frac{E_D}{2}$), because static Young's modulus is more appropriate for volcanic deformation timescales (Gudmundsson, 2011; Heap et al., 2020). The resulting range of static Young's moduli (E) is between approximately 1 and 100 GPa (Fig. 2) and appropriate for volcanic regions (Gudmundsson, 2020). The surrounding host rock is also assumed to be impermeable, with no permeability values attributed to it.

We assume a uniform distribution of crystals throughout the magma reservoir, with a constant porosity value of 0.3, derived from the maximum melt fraction from seismic tomography studies (Annen et al., 2014; Paulatto et al., 2012). We apply a steady melt injection rate at the reservoir base and then adjust this rate over time to optimize against the observed temporal pattern in the continuous GPS (cGPS) recordings. The melt injected does not account for a separate crystal phase which would impact its viscosity; we assume a bulk fluid viscosity based on published values (Table 1). The impact of different viscosity melt injections is explored in Alshembari et al. (2022a).

In this study we aim to constrain three different parameters: the depth of the reservoir inlet (D) and therefore the reservoir, the mush permeability (k), and the volumetric melt injection rate (Q). The depth of the reservoir inlet is critical due to the non-uniform pressure distribution within the reservoir from the poroelastic representation and melt injection from depth. In this case, the reservoir pressure is primarily concentrated around the injection location, which is different from melt-dominated reservoirs, or reservoirs represented as pressurized cavities, where the pressure is evenly distributed (Alshembari et al., 2022b; Hickey et al., 2016).

Hydraulic diffusivity depends on both permeability and melt viscosity (Eq. (1)). We assume a constant melt viscosity ($\eta_m = 1 \times 10^3 Pa\,\mathrm{sec}$) typical for mafic magma (Kilburn, 2000; Plail et al., 2014). This assumption is based on research suggesting the presence of mafic magmas at the Soufrière Hills Volcano (SHV), as evidenced by mafic enclaves within the extruded andesitic lava (Barclay et al., 2010; T E Christopher et al., 2015; Plail et al., 2018). Therefore, while focusing on estimating permeability values, we have used a fixed viscosity representative of mafic magmas.. We also assume a constant magma compressibility ($\beta_m = 1 \times 10^{-10}\,Pa^{-1}$) (Gottsmann and Odbert, 2014). The pressure evolution resulting from melt injection is a convolution of

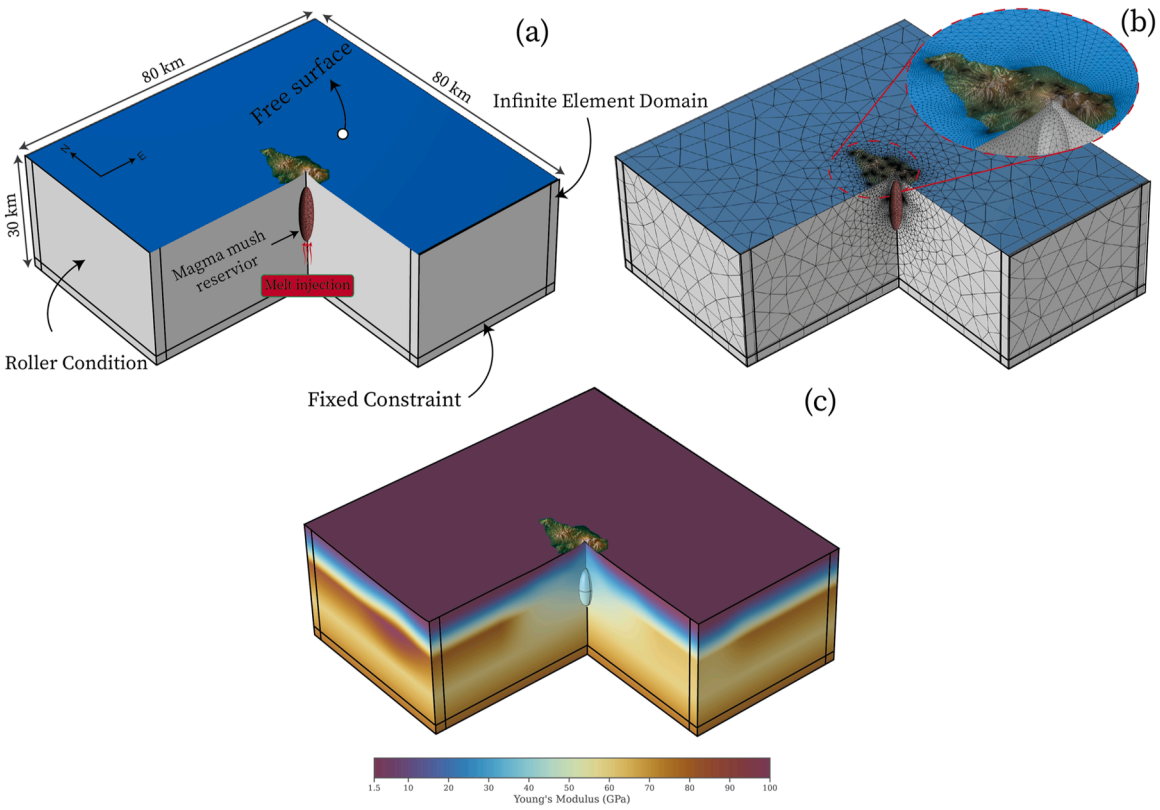

Fig. 2. Finite-element analysis model of surface deformation. (A) Geometry and applied boundary conditions (fixed, roller, free). (B) Meshed geometry with a close-up view of the island-wide meshing. (C) Three-dimensional distribution of static Young's modulus derived from seismic tomography data (Paulatto et al., 2012).

both the volumetric injection rate and the injected melt compressibility (Huppert and Woods, 2002; Kilbride et al., 2016). Changing melt compressibility values has a linear impact on the final constrained injection rate values (for instance, doubling the compressibility results in doubled injection rate values, accounting for increased volume compaction). We highlight that the outcomes of this study are influenced by the assumptions made in the analyses and discuss the impacts of this. A summary of the parameters is shown in Table 1.

2.3. Forward and inverse model approach

In the numerical modeling process we first performed ~15,000 forward models across three key parameters: permeability ($1 \times 10^{-12}\ m^2 \leq k \leq 1 \times 10^{-8}\ m^2$), reservoir inlet depth ($10\ km \leq D \leq 18\ km$), and volumetric injection rate ($0.1\ m^3 sec^{-1} \leq Q \leq 1\ m^3 sec^{-1}$), to help prevent the optimization from getting trapped in local minima and ensure a more comprehensive search for the global minimum (Fig. 3). In these models, we assume a constant inlet volumetric rate Q and focus on solving for the spatial deformation pattern. Subsequently, we calculate and minimize the misfit between the model predictions and the GPS data using the chi-squared (χ^2) statistic:

$$\chi^2 = \sum_{i=1}^{n} \left(\frac{O_i - u_i}{O_i} \right)^2, \tag{8}$$

where $n = 42$ is the number of GPS recordings of displacement (3 components $\times$ 14 stations $=$ 42 recordings), O_i is the GPS observed displacement and u_i is the displacement values obtained from the numerical models. We used the results to identify an initial confidence interval for each parameter within the region containing the 70 smallest χ^2 values.

Next, we employed a coordinate search iterative optimization method within the previously defined confidence interval to find a more optimal solution (Fig. 3). The Coordinate Search Solver is an iterative optimization method aimed at improving the objective function (χ^2) along the coordinate directions of the control parameter space without directly evaluating gradients (Frandi and Papini, 2014). It is particularly useful when gradients are not available or well-defined, such as with noisy objective functions. The method operates by starting with an initial guess in the parameter search space and systematically investigates one variable at a time. It assesses the objective function at a fixed distance along each coordinate axis in both positive and negative directions, updating the position if a better solution is identified (Frandi and Papini, 2014; Goertzel, 1992). The algorithm adjusts step lengths based on the objective function values and decreases the movement distance upon discovering a better minimum, ultimately searching for the optimal solution within the confidence interval (Conn et al., 2009; Frandi and Papini, 2014).

Once we obtain a more optimal value from the coordinate search, we repeat the first step (confidence interval identification) using the parameter values derived from the coordinate search as the initial guess to further minimize χ^2 (Fig. 3). A subsequent coordinate search optimization was conducted on the reservoir location variables (x_{loc} and y_{loc}) to further minimize the misfit between the model and observed data. Following that, we apply the coordinate search iterative optimization method again within the second confidence interval to identify our final optimal solution. Fig. 3 illustrates the modeling steps and the corresponding output for each stage.

After optimizing our fit to the spatial deformation pattern, we fit the displacement time series recordings by incorporating a time-varying inlet volumetric rate. We conduct a series of forward models with a time-varying inlet injection rate and investigate the best fit corresponding to the temporal evolution of the GPS vertical deformation. We apply a linearly decreasing function for the inlet volumetric flow rate, starting with an initial rate (Q_{i1}) and ending with a final rate (Q_{i2}) over a

Table 1
List of model parameters.

Variable	Definition	Dimensions	Value	Reference
Wall Rock parameters				
E	Young's modulus	GPa	1.6 – 86	(Paulatto et al., 2012)
v	Poisson's ratio	–	0.25	(Alshembari et al., 2022a)
ρ_r	Host rock density	$kg\ m^{-3}$	1650 - 3239	(Hickey et al., 2022)
Mush Reservoir parameters				
$\varnothing$	Mush porosity (melt fraction)	–	0.3	(Annen et al., 2014; Paulatto et al., 2019, 2012)
K_d	Bulk Modulus of the drained porous media	GPa	2.5	(Paulatto et al., 2012)
G_d	Shear Modulus of the drained porous media	GPa	1.6	(Paulatto et al., 2012)
v_d	Poisson's ratio of the drained porous media	–	0.25	(Paulatto et al., 2012)
K	Mush permeability	m^2	$1 \times 10^{-8} \leq 1 \times 10^{-12}$	
A	Biot-Willis coefficient	–	0.6	(Alshembari et al., 2022a)¶
Reservoir geometry Properties				
a	Reservoir semi-major axis	km	5	(Gottsmann et al., 2020b; Hickey et al., 2022)
b	Reservoir semi-intermediate axis	km	2	(Gottsmann et al., 2020b; Hickey et al., 2022)
c	Reservoir semi-minor axis	km	1.9	(Gottsmann et al., 2020b; Hickey et al., 2022)
D	Reservoir inlet depth / depth to base of reservoir	km	10 - 18	–
Melt properties				
η_m	Melt viscosity	Pa s	1×10^3	(Kilburn, 2000; Plail et al., 2014)
χ_m	Melt compressibility	Pa^{-1}	1×10^{-10}	(Gottsmann and Odbert, 2014; Kilbride et al., 2016)
Q_i	Melt injection volumetric rate	$m^3\ sec^{-1}$	0.1 – 1.2	

12-year period (2010–2022). The total volume of injected melt matches the volume of melt injected at a constant rate, which is derived from the prior deformation optimization against the spatial components of the GPS data. By fitting the observed GPS displacements, we can identify changes in melt injection rates over time, providing insights into the magmatic system's temporal dynamics.

2.4. cGPS data

We analyze GPS deformation data gathered from Soufrière Hills Volcano (SHV) during the ongoing intra-eruptive unrest period spanning from 2010 to 2022, collected by the Montserrat Volcano Observatory (MVO). We use recordings from a total of 20 GPS stations, with 14 continuous (cGPS) and 6 campaign (eGPS) stations. The campaign GPS stations have not been incorporated into our optimization process (Figs. 1, S1, and S2), due to their limited temporal resolution, but are compared to predicted model outputs. For the data inversion, we use displacements obtained from the total time-integrated and polynomially averaged three-components (Ux, Uy, and Uz) of the 14 cGPS stations (Figs. 1, S1, and S2).

Since 1995, continuous geodetic data have been gathered at SHV (Hickey et al., 2022; Odbert et al., 2014). The data set for the period from 2010 to 2022 is comprised of daily timeseries from up to 20 on-island GPS sites. Daily GPS data are initially converted into the RINEX format and then processed using the GAMIT/GLOBK software (Herring, 2015), which utilizes a double-differencing processing approach. In the GAMIT processing stage, baselines between GPS sites are computed in the ITRF14 coordinate system, excluding displacements caused by equipment changes . The GLOBK step calculated stable GPS station coordinates in a Caribbean reference frame to remove the regional tectonic component from the displacements (Hickey et al., 2022; Odbert et al., 2014).

3. Results and discussion

In this section, we will present the results obtained from the later stages of the optimisation process (Step 6 onwards in Fig. 3). The results from the previous steps (Steps 1–5) can be found in the Supplementary Material (Figs. S3–S5).

3.1. Global χ^2 optimization statistics

In step 6, the initial estimates for the parameters are derived from the results of the previous steps (Steps 1–5): the depth to the reservoir inlet (D) is 14.17 km, the inlet volumetric flow rate (Q_i) is 0.97 m^3/s, and the mush permeability (k) is 3×10^{-11} m^2. The initial estimates are used to constrain parameter value ranges for global χ^2 assessments (step 7) that produce our second confidence intervals in step 8 (Fig. 4).

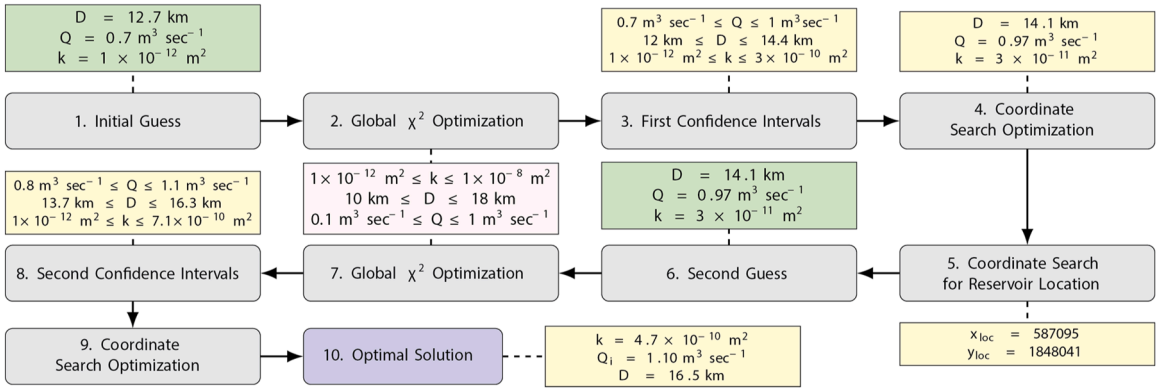

Fig. 3. Step-by-step flow chart illustrating the model formulation and the inverse problem. Each yello7w box displays the control parameter output results corresponding to the attached step in the process. The two green boxes represent the initial assumptions for each global χ^2 optimization process.

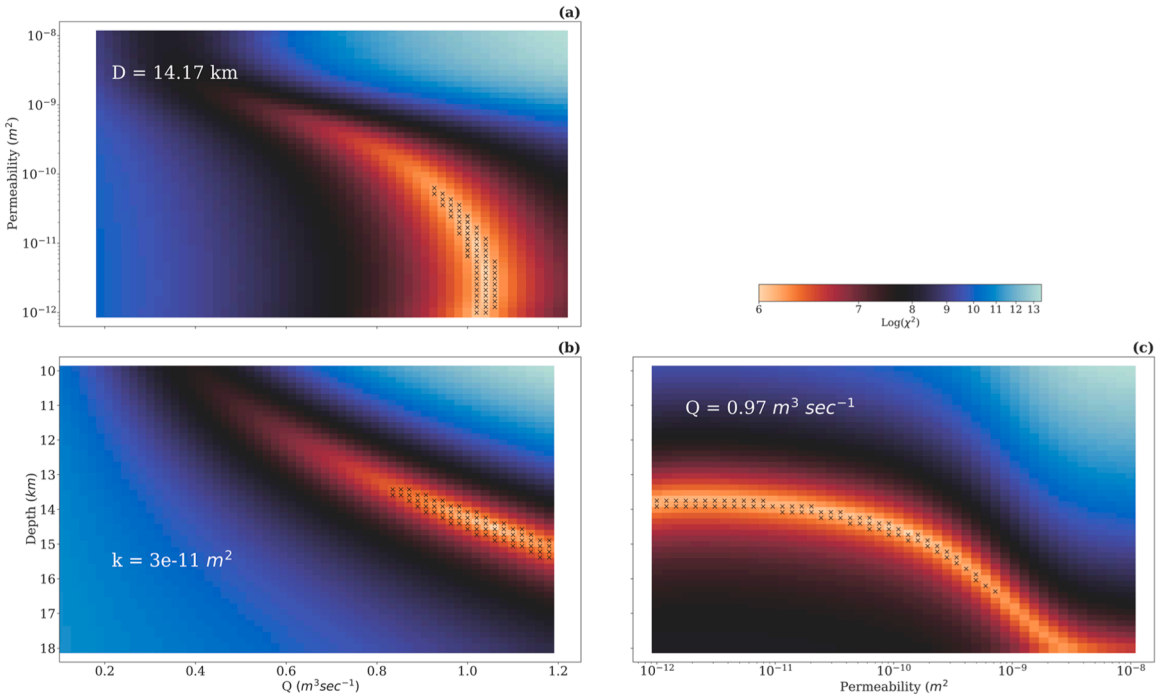

Fig. 4. Global χ^2 optimization of the three control parameters: reservoir inlet depth (D), mush permeability (k), and inlet volumetric flow rate (Q_i). (a) Log(χ^2) values of the combination between k and Q_i, (b) between D and Q_i, and (c) between D and k. χ^2 is calculated for each set of combinations by fixing the third parameter with the values displayed on each plot. The black crosses on each plot represent the 70 smallest χ^2 values for each analysis to define our confidence intervals.

The derived confidence intervals for the three study parameters are as follows: permeability ranging from 1×10^{-12} m^2 $\leq k \leq 7.19 \times 10^{-10}$ m^2, injection rate confined between 0.81 m^3 sec^{-1} $\leq Q_i \leq$ 1.18 m^3 sec^{-1}, and reservoir inlet depth spanning 13.75 km $\leq D \leq$ 16.3 km. These ranges were used as the inputs for the coordinate search to identify our optimal solution that further minimizes the χ^2 value. A notable observation from the global χ^2 estimation and confidence intervals is that when changing the permeability values below a certain threshold value, the χ^2 value does not change significantly (Fig. 4c). This is attributed to a low resultant diffusivity, which inhibits any substantial variations in the effective depth of the pressurized zone within the mush of the magma reservoir. The permeability threshold value is $k_{Thr} \approx 1 \times 10^{-11}$ m^2, at which point the χ^2 minimum value begins to bend as the other parameters change.

The three examined parameters are not entirely independent of each other. An increase in the injection rate Q leads to an increase in reservoir inlet depth D. However, these two parameters differently influence the deformation's spatial distribution. Specifically, Q primarily modifies the absolute magnitude of the deformation, while D affects both the magnitude and spatial pattern (i.e., footprint) of the deformation. In addition, it is important to consider the interplay between permeability and the effective depth of the reservoir. The effective depth represents the midpoint of the pressurized region within the mush reservoir, essentially reflecting the depth of the deformation source. As the permeability increases, it results in a decrease in the effective depth of the reservoir, i.e., the reservoir appears shallower as the greater permeability allows the melt to percolate further in a given time period, extending the area of melt / pressure accumulation. This, in turn, necessitates an increase in the depth of the reservoir inlet if intending to maintain a constant maximum deformation magnitude. Furthermore, an inverse relationship is observed when considering the injection rate and permeability. As the injection rate increases, the permeability tends to need to decrease. The increase in the effective depth of the reservoir acts as a compensatory mechanism, occurring in response to a decrease in mush permeability. This decrease of permeability limits melt diffusion, causing the melt to concentrate closer to the reservoir inlet and at greater depths, which in turn necessitates a higher injection rate to balance the resulting deformation.

3.2. Coordinate search optimization

We utilize a coordinate search optimization (step 9) within the confidence intervals derived from the global χ^2 evaluations (step 8) to further minimize the χ^2 value, ultimately identifying our optimal values for the three parameters. We considered a truncated range of permeability values, with the lower bound constrained by our threshold permeability identified previously: $1 \times 10^{-11} \leq k \leq 7.19 \times 10^{-10}$. Any lower permeability values also generate unrealistically high pressures ($\sim 1 \times 10^{12}$ *Pa*) at the melt injection reservoir entrance because of a low diffusivity. The coordinate search analysis shows that our minimum χ^2 is attained at the following parameters: $k = 4.7 \times 10^{-10}$ m^2, $Q_i = 1.1$ m^3 s^{-1}, and $D = 16.5$ km (Fig. 5). Our findings suggest that melt is injected into an extensive porous mush-dominated region, that extends from a depth of ~16.5 km to shallower depths (~ 6.5 km). The optimal solution provides a satisfactory fit for the deformation, particularly for the far-field stations such as NWBL, GERD, MVO1 and BNBY (Fig. 6). The misfit observed for the near-field stations (e.g., FRGR and HERM) may be attributed to shallow processes, such as compaction or deposit loading (Odbert et al., 2015), which cannot be easily differentiated from the magmatic processes involved, or due to shallower magmatic or hydrothermal processes not modelled in our study (Fig. 6) (Johnson et al., 2023).

3.3. Temporal variations in melt injection rates and hazard implications

The previous analysis considered a constant melt injection rate throughout the model simulation, resulting in a linear increase in surface deformation (Fig. S6). However, the cGPS deformation time series show a decreasing deformation rate (Fig. 1), suggesting that the magma injection rate may vary over time. To investigate this, we examine the time series from evenly distributed stations across the island (NWBL, OLVN, BNBY, AIRS, HARR, and SPRI) and fit the vertical deformation

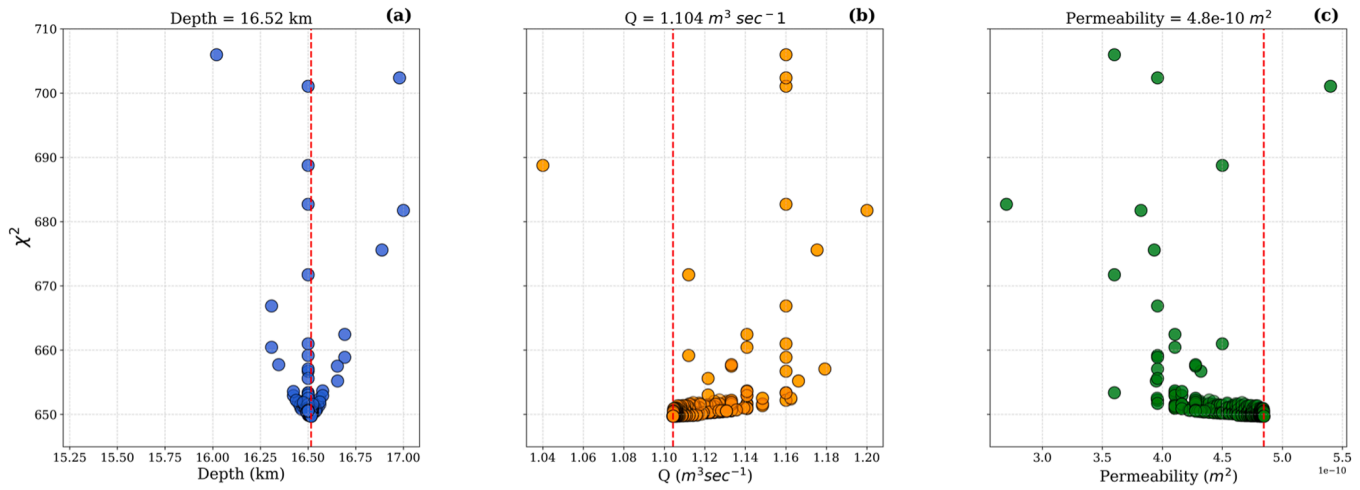

Fig. 5. Coordinate search optimization results obtained within the confidence intervals. (a) χ^2 values against reservoir inlet depth (D), (b) against volumetric inlet flow rate (Q), and (c) against mush permeability (k). The optimal solution, denoted by the minimum χ^2, is displayed at the top of each subplot and is represented by a vertical red dashed line.

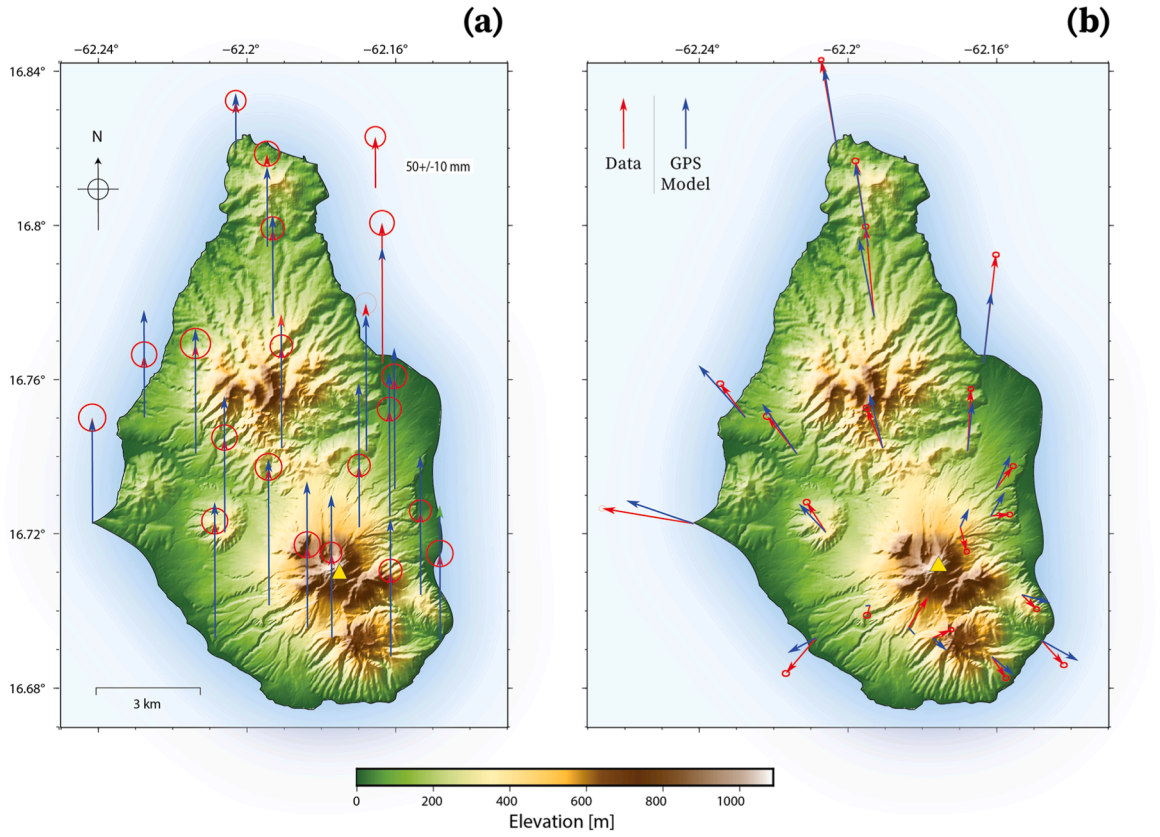

Fig. 6. Observed (red) and modeled displacements for GPS (blue) stations. (a) Vertical displacements. (b) Horizontal displacements. Red arrows represent observed deformation in both maps.

component with varying-inlet melt rate forward models. We consider a linearly decreasing function for the inlet volumetric flow rate, starting with an initial rate (Q_{i1}) and ending with a final rate (Q_{i2}) after 12 years (2010–2022). The flow rate decreases with a slope ($s = (Q_{i2} - Q_{i1})/12$); the total volume of injected melt equals the melt volume (0.42 km^3) injected at a constant rate $Q_c = 1.1042\, m^3\, sec^{-1}$, obtained from the prior deformation optimization against the spatial components of the GPS data. The estimation of the injected magma volume is based on the assumption of constant magma compressibility, a value that is based on ranges reported in the literature (Huppert and Woods, 2002; Kilbride et al., 2016). Consequently, the confidence in the total volume estimated is linked to the compressibility assumption.

The time series of deformation data suggests a decreasing trend in the melt rate over time. Our best-fit value for the initial injection rate is $Q_{i1} = 1.9\, m^3\, sec^{-1}$ and for the final injection rate is $Q_{i2} = 0.3\, m^3\, sec^{-1}$. These values produce model outputs that match the observed GPS deformation timeseries. The vertical component of the deformation is demonstrated in Figs. 7, S7 and S8 respectively illustrate the N-S and E-

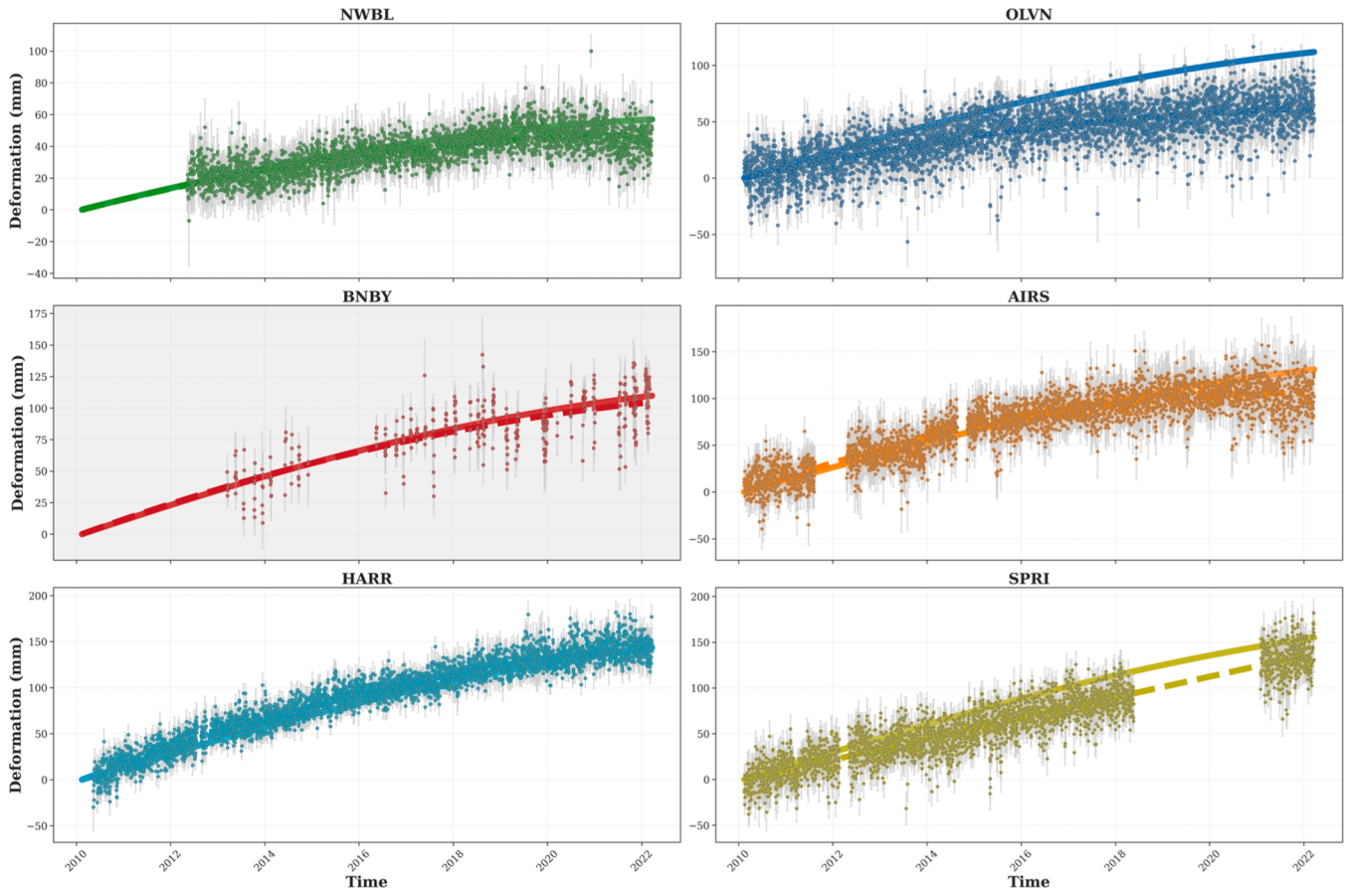

Fig. 7. Comparison of observed vertical deformation time-series and modelled deformation resulting from a decreasing melt injection rate. The dashed lines represent the polynomial fitting of the observed vertical deformation (coloured dots) at each station, while the solid lines display the modelled deformation results. GPS station names are indicated above the plots.

W components. Some absolute values still show misfits at the end of the model simulation (similar to the misfits in Fig. 6 due to the same volume of melt being intruded), but the time-dependent decrease in deformation rate is captured well in all cases.

If the decreasing melt injection rate we constrain for the currently recorded GPS period (2010–2022) continues to decline at the same rate, the melt supply would be projected to likely stop by June 2024. However, the system continues to evolve and deform even when the melt supply has stopped (Fig. 8) due to the poroelastic melt diffusion process within the magma reservoir (Alshembari et al., 2022a). As an alternative scenario, we also examined the predicted deformation if the melt supply linearly decreases and then stops abruptly at end of the GPS recording date (t_{end} = 02/2022). Additionally, we analysed scenarios with greater initial melt supply rates and faster decreases in melt supply, such that the total injected volume is still the same but the injection stops either 4 or 6 years after the model start (t_{end} = 2014 and 2018) (Fig. 8). Similarly, our results indicate that the system will continue to evolve and deform for all the considered scenarios after the melt injection has stopped due to the poroelastic diffusion of melt from the injection point to the margins of the magma reservoir. By comparing the various scenarios to the GPS timeseries, the best fits are provided by the initial two scenarios (Fig. 8, green and red lines). Increasing the initial melt supply rate and

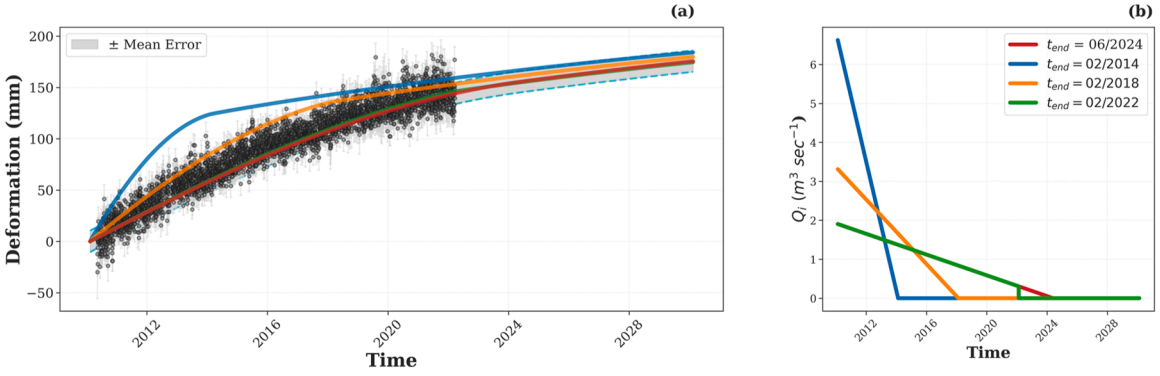

Fig. 8. Comparison of observed time-series vertical deformation and extended modeled vertical deformation at HARR station. The two solid lines represent the modeled deformation results from the two different inlet functions shown in (b). The grey area surrounding the modeled deformation indicates the mean error from the recordings at the HARR station.

ending the melt supply period earlier produces deformation rates that are initially too high, and then eventually too slow once the melt diffusion process becomes the dominant force in driving surface deformation (Fig. 8, blue and orange lines). Importantly, these results imply that melt supply has been ongoing from 2010 to at least 2022, supporting the findings of simpler models and the assertion that the current repose period should continue to be classified as intra-eruptive (Hickey et al., 2022).

The modelled deformation from the continued melt injection case (red line) and the earlier injection termination case (t_{end}=02/2022, green line) are very similar (Fig. 8). The high degree of similarity is because the deformation created after the two volume injection rate profiles diverge (02/2022) is dominated by poroelastic melt diffusion rather than the melt injection process, as the melt injection rate has become insignificantly small.

We performed a further sensitivity analysis to determine a potential window for the termination of melt supply. We consider a time window that spans before and after the previously presumed point of melt cessation to help us identify the uncertainty around the likely end of the melt supply. Our findings indicate a melt supply termination window of 06/2024 $\pm$ 2 years (Fig. 9). Pinpointing a more exact time for the end of melt supply is complex due to the interplay between the melt injection and the melt diffusion process within the mush.

These findings impact our understanding of volcanic hazards at SHV and can help inform volcano monitoring strategies. If the melt supply has ceased and can be identified by the much-reduced rate of surface deformation (Fig. 9) it might indicate a reduction in volcanic hazard, and possibly the end of the current eruptive episode. However, caution must be taken as the end of melt supply does not imply the complete absence of potential hazards. Continued porous melt diffusion could still lead to accumulation of mobile melt and reservoir pressurisation, which could theoretically contribute to mechanical failure of the reservoir and dyke formation to possibly feed magma ascent and renewed eruption. Crucially, as the rate of deformation slows down, it might become increasingly challenging to detect using standard geodetic methods. Understanding the point at which the deformation rate may signal the end of melt supply is important for interpreting monitoring data and anticipating changes in volcanic activity. After the melt supply has stopped the deformation at GPS station HARR may continue at a rate of 4 mm/yr (Fig. 9). Therefore, continued monitoring of volcanic signals combining a variety of techniques, even during periods of low activity, remains essential.

3.4. Model limitations

Our study, despite its comprehensive approach to understanding the dynamics of SHV, possesses certain inherent limitations due to the novelty of our approach. A major aspect of these limitations relates to the intricate interplay between magma compressibility, the Biot-Willis poroelastic coefficient, and mush porosity. These parameters are interconnected and collectively affect the final determined volumetric injection rate. To make our model more robust, integrating more petrological and geochemical studies could serve to constrain some of these parameters independently, which is scarce at the time of this study. Another complexity arises from the interdependency between melt viscosity and permeability. Both modify the hydraulic characteristics of the mush. To improve this in our model, further geophysical studies should aim at independently constraining either of these parameters.

The reservoir dimensions in our study were determined based on previous geodetic studies of SHV (Gottsmann et al., 2020a; Hickey et al., 2022; Johnson et al., 2023). However, these studies are primarily based on solid-mechanics only models simulated with a uniformly pressurized prolate ellipsoid cavity, which may be in contradiction with the dynamic mush-dominated hypothesis used in our study. Future work may benefit from aiming to optimize a reservoir geometry when employing a coupled, dynamic, solid and fluid mechanics approach with a poroelastic reservoir. Our study also considered a constant and uniform porosity and crystal distribution throughout the magma reservoir, which is a simplification, especially when considering the potential temperature variations throughout the reservoir that could cause non-uniform crystal distributions. The porosity distribution aspect of our model could be refined by incorporating additional thermal models that more accurately quantify the spatial and temporal distribution of crystals.

Our model assumes that the reservoir and the surrounding rock have elastic rheology. However, the heated host rock and the mush might be more accurately represented by a thermo-viscoelastic and poroviscoelastic material, respectively. While the poroviscoelastic aspect of the reservoir may not be important for surface deformation modeling, a thermo-viscoelastic host rock in parallel with a poroelastic reservoir has been shown to influence syn- and post-injection temporal deformation (Alshembari et al., 2023). In the thermo-viscoelastic host rock, there tends to be a tendency towards subsidence caused by the stress relaxation over time. On the other hand, poroelastic mush rheology generally leads to rate-decreasing uplift rates caused by the melt diffusion in the mush. Incorporating these additional rheologies while also testing our models against observed data was beyond the scope of this study.x

Finally, we considered the deformation to be solely caused by magmatic intrusion. Nonetheless, various other processes like changes in hydrothermal systems (Fournier and Chardot, 2012), the cooling and crystallization of a magmatic reservoir (Parker et al., 2014), and the loading of volcanic deposits (Odbert et al., 2015) can cause surface deformation. Addressing our limitations in future research could offer a further nuanced insight into the deformation and melt dynamics of SHV

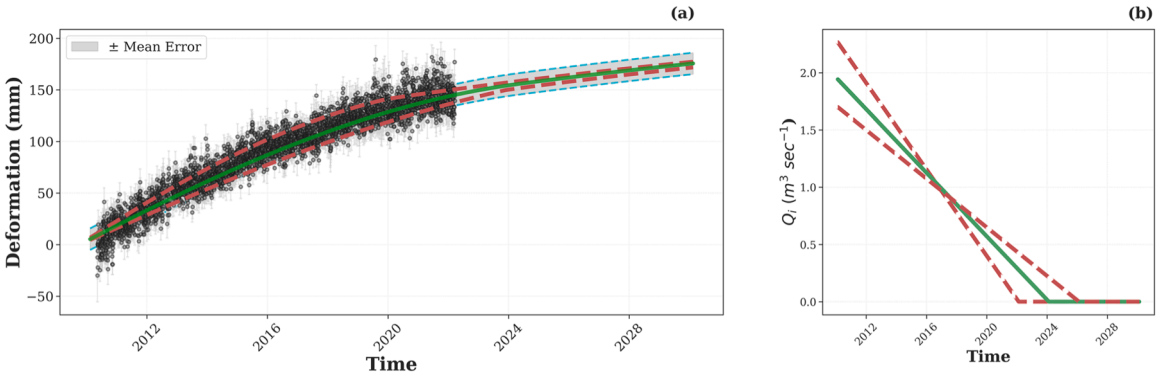

Fig. 9. Comparison of observed vertical deformation time-series and extended modeled vertical deformation at HARR station. The solid green lines represent the modeled deformation results from the scenario in which the injection source continue to decrease linearly at a consistent rate throughout the entire recording time, coming to a complete halt by June 2024. The two dashed lines represent the deformation caused by two injection functions, one terminating two years prior and the other two years after the case denoted by the green line.

and other similar volcanic systems.

4. Conclusions

Our work has explored the deformation dynamics of SHV, shifting the focus towards a mush-dominated magma reservoir, modelled as a poroelastic medium. Our results suggest that the 2010–2022 deformation at SHV is driven by ongoing, melt injection into the base of a mush-based reservoir (D = 16.5 km, Q = 1.1 m^3 sec^{-1}) of relatively low permeability ($k = 4.7 \times 10^{-16}$ m^2). The emphasis on the mush reservoir adds a novel dimension to our understanding of SHV dynamics and the associated deformation. We also constrain a temporal variation in the melt injection rate, as evidenced by decreasing-rate surface deformation recorded at the GPS stations. The initial higher injection rate of $Q_i = 1.9$ m^3 sec^{-1} at the start of our observations (2010) reduces to $Q_f = 0.3$ m^3 sec^{-1} over a 12-year period. The decline in melt injection rate leads to decreased surface deformation rates, and a transition from deformation being initially driven by melt supply to subsequently being dominated by a melt diffusion process within the reservoir. The transition in process driving magma migration may have changing hazard implications for the volcano.

Exploring possible future behavior based on these findings, we estimate melt supply to the modelled reservoir could finish around June 2024 ± 2 years. However, a potential cease of new magma supply does not equate to a completely diminished hazard assessment. Even in the absence of active melt intrusion, the secondary process of poroelastic melt diffusion continues to play a role in ongoing deformation and magma migration, accumulation, and pressurisation. It is feasible this process could lead to further stress accumulation in the mush reservoir and potentially cause it to rupture and allow magma to reach the surface.

Our study highlights the need for continuous monitoring of the volcano, even in the face of a slowing or ceased melt supply, as the complex dynamics of a mush-dominated reservoir can still present hazards.

CRediT authorship contribution statement

Rami Alshembari: Writing – review & editing, Writing – original draft, Visualization, Validation, Software, Resources, Project administration, Methodology, Investigation, Formal analysis, Data curation, Conceptualization. **James Hickey:** Writing – review & editing, Writing – original draft, Supervision, Software, Conceptualization. **Karen Pascal:** Writing – review & editing, Data curation. **Racquel Syers:** Data curation.

Declaration of competing interest

The authors declare that they have no known competing financial interests or personal relationships that could have appeared to influence the work reported in this paper.

Data availability

The data supporting this study can be acquired from the Montserrat Volcano Observatory (MVO) upon a collaboration agreement.

Acknowledgments

Rami Alshembari is grateful to the University of Exeter for funding his PhD studentship.

References

Alshembari, R., Hickey, J., Williamson, B.J., Cashman, K., 2023. Unveiling the rheological control of magmatic systems on volcano deformation: the interplay of poroviscoelastic magma-mush and thermo-viscoelastic crust. J. Geophys. Res. Solid Earth 128, 1–16. https://doi.org/10.1029/2023JB026625.

Alshembari, R., Hickey, J., Williamson, B.J., Cashman, K., 2022a. Poroelastic mechanical behavior of crystal mush reservoirs: insights into the spatio-temporal evolution of volcano surface deformation. J. Geophys. Res. Solid Earth 127. https://doi.org/10.1029/2022JB024332.

Alshembari, R., Hickey, J., Williamson, B.J., Cashman, K., 2022b. Exploring the role of fluid-solid interactions for modelling volcano deformation. J. Volcanol. Geotherm. Res. 426, 107535 https://doi.org/10.1016/j.jvolgeores.2022.107535.

Annen, C., Paulatto, M., Sparks, R.S.J., Minshull, T.A., Kiddley, E.J., 2014. Quantification of the intrusive magma fluxes during magma chamber growth at soufrière hills volcano (montserrat, Lesser Antilles). J. Petrol. 55, 529–548. https://doi.org/10.1093/petrology/egt075.

Bachrach, R., 2011. Poroelasticity. Encyclopedia of Earth Sciences Series, pp. 1003–1005. https://doi.org/10.1007/978-90-481-8702-7_26.

Barclay, J., Herd, R.A., Edwards, B.R., Christopher, T., Kiddle, E.J., Plail, M., Donovan, A., 2010. Caught in the act: implications for the increasing abundance of mafic enclaves during the recent eruptive episodes of the Soufrière Hills Volcano, Montserrat. Geophys. Res. Lett. 37 https://doi.org/10.1029/2010gl042509 n/a-n/a.

Biot, M.A., 1941. General theory of three-dimensional consolidation. J. Appl. Phys. 12, 155–164. https://doi.org/10.1063/1.1712886.

Brocher, T.M., 2005. Empirical relations between elastic wavespeeds and density in the Earth's Crust. Bull. Seismol. Soc. Am. 95, 2081–2092. https://doi.org/10.1785/0120050077.

Cashman, K.V., Sparks, R.S.J., Blundy, J.D., 2017. Vertically extensive and unstable magmatic systems: a unified view of igneous processes. Science (80-.) 355, eaag3055. https://doi.org/10.1126/science.aag3055.

Cayol, V., Peltier, A., Froger, J., Beauducel, F., 2022. Monitoring volcano deformation. In: Hazards and Monitoring of Volcanic Activity, 2. Wiley, pp. 95–165. https://doi.org/10.1002/9781394169610.ch2.

Christopher, T.E., Blundy, J., Cashman, K., Cole, P., Edmonds, M., Smith, P.J., Sparks, R. S.J., Stinton, A., 2015. Crustal-scale degassing due to magma system destabilization and magma-gas decoupling at Soufrière Hills Volcano, Montserrat. Geochem., Geophys. Geosyst. 16, 2797–2811. https://doi.org/10.1002/2015GC005791.

Conn, A.R., Scheinberg, K., Vicente, L.N., 2009. Introduction to derivative-free optimization. Soc. Indus. Appl. Math. https://doi.org/10.1137/1.9780898718768.

Detournay, E., Cheng, A.H., 1994. Fundamentals of poroelasticity. Int. J. Rock Mech. Min. Sci. Geomech. Abstr. 31, 138–139. https://doi.org/10.1016/0148-9062(94)90606-8.

Devine, J.D., Rutherford, M.J., 2014. Chapter 19 Magma storage region processes of the Soufrière Hills Volcano, Montserrat. Geol. Soc. London, Mem. 39, 361–381. https://doi.org/10.1144/m39.19.

Dzurisin, D., 2006. Volcano Deformation. Springer Berlin Heidelberg, Berlin, Heidelberg. https://doi.org/10.1007/978-3-540-49302-0.

Edmonds, M., Cashman, K.V., Holness, M., Jackson, M., 2019. Architecture and dynamics of magma reservoirs. Philos. Trans. R. Soc. A Math. Phys. Eng. Sci. 377 https://doi.org/10.1098/rsta.2018.0298.

Edmonds, M., Kohn, S.C., Hauri, E.H., Humphreys, M.C.S., Cassidy, M., 2016. Extensive, water-rich magma reservoir beneath southern Montserrat. Lithos 252–253, 216–233. https://doi.org/10.1016/j.lithos.2016.02.026.

Elsworth, D., Mattioli, G., Taron, J., Voight, B., Herd, R., 2008. Implications of magma transfer between multiple reservoirs on eruption cycling. Science (80-.) 322, 246–248. https://doi.org/10.1126/science.1161297.

Fournier, N., Chardot, L., 2012. Understanding volcano hydrothermal unrest from geodetic observations: insights from numerical modeling and application to White Island volcano, New Zealand. J. Geophys. Res. Solid Earth 117, 1–16. https://doi.org/10.1029/2012JB009469.

Frandi, E., Papini, A., 2014. Coordinate search algorithms in multilevel optimization. Optim. Method. Softw. 29, 1020–1041. https://doi.org/10.1080/10556788.2013.841691.

Goertzel, B., 1992. Global optimization by multilevel search. J. Optim. Theory Appl. 75, 423–432. https://doi.org/10.1007/BF00941477.

Gottsmann, J., Flynn, M., Hickey, J., 2020a. The transcrustal magma reservoir beneath Soufrière Hills Volcano, montserrat: insights from 3-D geodetic inversions. Geophys. Res. Lett. 47 https://doi.org/10.1029/2020GL089239.

Gottsmann, J., Flynn, M., Hickey, J., Odbert, H., 2020b. The transcrustal magma reservoir beneath Soufrière Hills Volcano, Montserrat: insights from 3-D geodetic inversions. J. Geophys. Res. Solid Earth 119, 4626–4639. https://doi.org/10.1029/2020GL089239.

Gottsmann, J., Odbert, H., 2014. The effects of thermomechanical heterogeneities in island arc crust on time-dependent preeruptive stresses and the failure of an andesitic reservoir. J. Geophys. Res. Solid Earth 119, 4626–4639. https://doi.org/10.1002/2014JB011079.

Gudmundsson, A., 2020. Volcanotectonics, Volcanotectonics. Cambridge University Press. https://doi.org/10.1017/9781139176217.

Gudmundsson, A., 2011. Rock Fractures in Geological Processes, Environmental & Engineering Geoscience. Cambridge University Press, Cambridge. https://doi.org/10.1017/CBO9780511975684.

Heap, M.J., Villeneuve, M., Albino, F., Farquharson, J.I., Brothelande, E., Amelung, F., Got, J.L., Baud, P., 2020. Towards more realistic values of elastic moduli for volcano modelling. J. Volcanol. Geotherm. Res. 390, 106684 https://doi.org/10.1016/j.jvolgeores.2019.106684.

Herring, T.A., 2015. Geodesy: an introduction and overview. Treatise On Geophysics. Elsevier, pp. 1–8. https://doi.org/10.1016/B978-0-444-53802-4.00055-5.
Hickey, J., Gottsmann, J., Nakamichi, H., Iguchi, M., 2016. Thermomechanical controls on magma supply and volcanic deformation: application to Aira caldera, Japan. Sci. Rep. 6, 32691. https://doi.org/10.1038/srep32691.
Hickey, J., Pascal, K., Head, M., Gottsmann, J., Fournier, N., Hreinsdottir, S., Syers, R., 2022. Magma pressurization sustains ongoing eruptive episode at dome-building Soufrière Hills Volcano, Montserrat. Geology 50, 1261–1265. https://doi.org/10.1130/G50239.1.
Huppert, H.E., Woods, A.W., 2002. The role of volatiles in magma chamber dynamics. Nature 420, 493–495. https://doi.org/10.1038/nature01211.
Johnson, A., Hickey, J., Pascal, K., Williamson, B.J., Syers, R., 2023. Distinguishing shallow from mid-crustal magmatic processes at Soufrière Hills Volcano using Finite Element Modelling and co-analysis of EDM and GPS data. Volcanica 6, 265–282. https://doi.org/10.30909/vol.06.02.265282.
Kilbride, B.M.C., Edmonds, M., Biggs, J., 2016. Observing eruptions of gas-rich compressible magmas from space. Nat. Commun. 7, 1–8. https://doi.org/10.1038/ncomms13744.
Kilburn, C.R.J., 2000. Lava flows and flow fields. Encycl. Volcanoe. 291–305.
Liao, Y., Soule, S.A., Jones, M., 2018. On the mechanical effects of poroelastic crystal mush in classical magma chamber models. J. Geophys. Res. Solid Earth 123, 9376–9406. https://doi.org/10.1029/2018JB015985.
Manga, M., 2018. Introduction to Poroelasticity Divid, p. 14.
Marsh, 1981. On the crystallinity, probability of occurrence, and rheology of lava and magma. Contrib. to Mineral. Petrol. 78, 85–98. https://doi.org/10.1007/BF00371146.
Mullet, B., Segall, P., 2022. The surface deformation signature of a transcrustal, crystal mush-dominant magma system. J. Geophys. Res. Solid Earth 127. https://doi.org/10.1029/2022JB024178.
Odbert, H., Ryan, G.A., Mattioli, G.S., Hautmann, S., Gottsmann, J., Fournier, N., Herd, R.A., 2014. Chapter 11 Volcano geodesy at the Soufrière Hills Volcano, Montserrat: a review. Geol. Soc. London, Mem. 39, 195–217. https://doi.org/10.1144/m39.11.
Odbert, H., Taisne, B., Gottsmann, J., 2015. Deposit loading and its effect on co-eruptive volcano deformation. Earth Planet. Sci. Lett. 413, 186–196. https://doi.org/10.1016/j.epsl.2015.01.005.
Parker, A.L., Biggs, J., Lu, Z., 2014. Investigating long-term subsidence at Medicine Lake Volcano, CA, using multitemporal InSAR. Geophys. J. Int. 199, 844–859. https://doi.org/10.1093/gji/ggu304.
Paulatto, M., Annen, C., Henstock, T.J., Kiddle, E., Minshull, T.A., Sparks, R.S.J., Voight, B., 2012. Magma chamber properties from integrated seismic tomography and thermal modeling at Montserrat. Geochem. Geophys. Geosystems 13, 1–18. https://doi.org/10.1029/2011GC003892.
Paulatto, M., Hooft, E.E.E., Chrapkiewicz, K., Heath, B., Toomey, D.R., Morgan, J.V., 2022. Advances in seismic imaging of magma and crystal mush. Front. Earth Sci. 10, 1–31. https://doi.org/10.3389/feart.2022.970131.
Paulatto, M., Moorkamp, M., Hautmann, S., Hooft, E., Morgan, J.V., Sparks, R.S.J., 2019. Vertically extensive magma reservoir revealed from joint inversion and quantitative interpretation of seismic and gravity data. J. Geophys. Res. Solid Earth 124, 11170–11191. https://doi.org/10.1029/2019JB018476.
Phillipson, G., Sobradelo, R., Gottsmann, J., 2013. Global volcanic unrest in the 21st century: an analysis of the first decade. J. Volcanol. Geotherm. Res. 264, 183–196. https://doi.org/10.1016/j.jvolgeores.2013.08.004.
Plail, M., Barclay, J., Humphreys, M.C.S., Edmonds, M., Herd, R.A., Christopher, T.E., 2014. Chapter 18 characterization of mafic enclaves in the erupted products of Soufrière Hills Volcano, Montserrat, 2009 to 2010. Geol. Soc. London, Mem. 39, 343–360. https://doi.org/10.1144/m39.18.
Plail, M., Edmonds, M., Woods, A.W., Barclay, J., Humphreys, M.C.S., Herd, R.A., Christopher, T., 2018. Mafic enclaves record syn-eruptive basalt intrusion and mixing. Earth Planet. Sci. Lett. 484, 30–40. https://doi.org/10.1016/j.epsl.2017.11.033.
Pritchard, M.E., Mather, T.A., McNutt, S.R., Delgado, F.J., Reath, K., 2019. Thoughts on the criteria to determine the origin of volcanic unrest as magmatic or non-magmatic. Philos. Trans. R. Soc. A Math. Phys. Eng. Sci. 377, 20180008 https://doi.org/10.1098/rsta.2018.0008.
Rosenberg, C.L., Handy, M.R., 2005. Experimental deformation of partially melted granite revisited: implications for the continental crust. J. Metamorph. Geol. 23, 19–28. https://doi.org/10.1111/j.1525-1314.2005.00555.x.
Rutter, E.H., Neumann, D.H.K., 1995. Experimental deformation of partially molten Westerly granite under fluid-absent conditions, with implications for the extraction of granitic magmas. J. Geophys. Res. Solid Earth 100, 15697–15715. https://doi.org/10.1029/94JB03388.
Segall, P., 2019. Magma chambers: what we can, and cannot, learn from volcano geodesy. Philos. Trans. R. Soc. A Math. Phys. Eng. Sci. 377, 20180158 https://doi.org/10.1098/rsta.2018.0158.
Segall, P., 2013. Volcano deformation and eruption forecasting. Geol. Soc. London, Spec. Publ. 380, 85–106. https://doi.org/10.1144/SP380.4.
Segall, P., 2010. Earthquake and volcano deformation. Choice Rev. Online 48. https://doi.org/10.5860/CHOICE.48-0287, 48-0287-48–0287.
Sparks, R.S.J., Annen, C., Blundy, J.D., Cashman, K.V., Rust, A.C., Jackson, M.D., 2019. Formation and dynamics of magma reservoirs. Philos. Trans. R. Soc. A Math. Phys. Eng. Sci. 377, 20180019 https://doi.org/10.1098/rsta.2018.0019.
Stinton, A.J., 2015. A new digital elevation model of the Soufrière Hills Volcano, Montserrat. MVO Open File Rep. 18 https://doi.org/10.13140/RG.2.1.2952.2809, 15–01.
Wadge, G., Voight, B., Sparks, R.S.J., Cole, P.D., Loughlin, S.C., Robertson, R.E.A., 2014. An overview of the eruption of Soufrière Hills Volcano, Montserrat from 2000 to 2010. Geol. Soc. Mem. 39, 1–39. https://doi.org/10.1144/M39.1.
Zellmer, G.F., Sparks, R.S.J., Hawkesworth, C.J., Wiedenbeck, M., 2003. Magma emplacement and remobilization timescales beneath Montserrat: insights from Sr and Ba zonation in plagioclase phenocrysts. J. Petrol. 44, 1413–1431. https://doi.org/10.1093/petrology/44.8.1413.